Giant quadratic magneto-optical response of thin $Y_3Fe_5O_{12}$ films for sensitive magnetometry experiments

E. Schmoranzerová,[1] T. Ostatnický,[1] J. Kimák,[1] D. Kriegner,[2,3] H. Reichlová,[2,3] R. Schlitz,[3] A. Baďura,[1] Z. Šobáň,[2] M. Münzenberg,[4] G. Jakob,[5] E.-J. Guo,[5] M. Kläui,[5] and P. Němec[1]

[1]*Faculty of Mathematics and Physics, Charles University, Prague, 12116, Czech Republic*
[2]*Institute of Physics ASCR v.v.i., Prague 162 53, Czech Republic*
[3]*Technical University Dresden, 01062 Dresden, Germany*
[4]*Institute of Physics, Ernst-Moritz-Arndt University, 17489 Greifswald, Germany*
[5]*Institute of Physics, Johannes Gutenberg University Mainz, 55099 Mainz, Germany*

(Received 26 October 2021; revised 17 August 2022; accepted 16 September 2022; published 30 September 2022)

We report an observation of a giant magneto-optical (MO) effect quadratic in magnetization (Cotton-Mouton effect) in a 50 nm thick layer of yttrium-iron garnet (YIG). By a combined theoretical and experimental approach, we managed to quantify both linear and quadratic MO effects in the studied material. We show that the quadratic MO signal in the thin YIG film can exceed the linear MO response, reaching values of 450 μrad that are comparable with Heusler alloys or ferromagnetic semiconductors. This relative enhancement of the quadratic MO response relative to the linear MO response is attributed to antiferromagnetic coupling of two Fe sublattices. Furthermore, we demonstrate that a proper choice of experimental conditions, particularly with respect to the used wavelength, is crucial for optimization of the quadratic MO effect, which can be used very efficiently for magnetometry measurement.

DOI: 10.1103/PhysRevB.106.104434

I. INTRODUCTION

Yttrium iron garnet ($Y_3Fe_5O_{12}$, YIG) is a prototype ferrimagnetic insulator which represents one of the key systems for modern spintronic applications [1]. This material has been thoroughly studied in recent decades owing to its special properties, such as low Gilbert damping [2–4] and high spin pumping efficiency [5–8]. YIG has played a crucial role in fundamental spintronics experiments, revealing spin Hall magnetoresistance [9,10] or spin-Seebeck effect [11–13].

Many of the above-mentioned spintronic phenomena rely on high-quality ultrathin YIG films and on detection of small changes in magnetization therein. However, YIG is a complex magnetic system with 200 μ_B magnetic moments per unit cell. Magnetic properties of the few monolayer systems used in spintronics are vulnerable to small structural changes and they are relatively difficult to characterize and control [14–17]. Moreover, reliability of conventional magnetometry tools, such as the superconducting quantum interference device (SQUID) or vibrating sample magnetometry (VSM), is limited by the large paramagnetic background and unavoidable impurity content of the gadolinium-gallium garnet that is commonly used as a substrate for the thin YIG layers. Direct use of magnetotransport methods for magnetic characterization is naturally prevented by a small electric conductivity of the insulating YIG. Magnetotransport can be utilized only indirectly in multilayers of YIG/heavy metal, via spin Hall magnetoresistance [17].

In contrast, optical interactions are not governed by DC conductivity of the material. Magneto-optics provides a natural tool for detection of the magnetic state of ferrimagnetic insulators. YIG in particular has an extremely strong magneto-optical response that can be easily modified by doping [18]. Magneto-optical (MO) response of a material manifests generally as a change of polarization state of a transmitted or reflected light [18], usually detected in the form of a rotation of the polarization plane of a linearly polarized light. Similar to the magnetotransport effects, MO effects with different symmetries with respect to magnetization ($\boldsymbol{M}$) can occur. Within certain limitations [19], an MO analogy to the anomalous Hall effect (AHE), which is linear in $\boldsymbol{M}$, is the Faraday effect in transmission geometry or the Kerr effect in reflection. For anisotropic magnetoresistance (AMR) quadratic in $\boldsymbol{M}$, the corresponding MO effect is magnetic linear dichroism (MLD) [19]. As the terminology is quite ambiguous in magneto-optics, MLD, Q-MOKE, Voigt, or Cotton-Mouton effect, which are sometimes used, all refer to the same phenomenon in different experimental geometries. In this paper, we have chosen to use the name "Cotton-Mouton effect" (CME) for the rotation of the polarization plane in transmission geometry that is quadratic in $\boldsymbol{M}$, consistent with the previous works performed on YIG [20,21]. Similarly, a variety of names is used in linear magneto-optics. As the usual Kerr or Faraday effects are observed in experimental geometries different from ours, we define the linear magneto-optical effect in transmission (LMET) in this work.

Quadratic MO effects scale with the square of magnetization magnitude and their symmetry is given by an axis parallel to the magnetization vector. As such, they are

generally weaker than the linear MO response [18]. However, there are significant advantages over the linear magneto-optics, making them favorable in MO magnetometry. The even symmetry with respect to the local magnetization enables one to observe these effects in systems with no net magnetic moment, such as collinear antiferromagnets, as the contributions from different sublattices do not cancel out [22]. Quadratic MO effects are sensitive to the angle between magnetization and the polarization plane [23], similarly to the way AMR is sensitive to the angle between magnetization and the electric current [19], which enables one to trace all the in-plane components of magnetization vector simultaneously in one experiment [23–26]. There is, however, one key advantage of the MO approach. The orientation of linear optical polarization can be set easily, unlike the current direction in the AMR measurement, which is defined by the electrical contact geometry. Consequently, variation of the light polarization provides an access to magnetocrystalline anisotropies [25] without modification of the sample properties by lithography, which is typically needed for the experimental methods based on electron transport.

In certain classes of materials and compounds with significant spin-orbit coupling, such as Heusler alloys [27] and ferromagnetic semiconductors [23,28], or some collinear [22] and noncollinear [29] antiferromagnets, the quadratic MO response can be strongly enhanced. There, the quadratic magneto-optics has found its important applications in static and dynamic MO magnetometry [28,30], helping to discover unique physical phenomena such as optical spin transfer [31] and spin-orbit torques [32]. In contrast, in ferrimagnetic insulators the quadratic MO effects have been vastly neglected so far. The first pioneering experiments have revealed the potential of the quadratic magneto-optics in YIG to visualize stress waves [33] or current-induced spin-orbit torque [21]. The inverse quadratic Kerr effect has even been identified as a trigger mechanism for ultrafast magnetization dynamics in thin YIG films [21]. However, no optimization of the MO effects was performed in these works in terms of their amplitude, spectral dependence, dependence on the angle of incidence, or initial polarization. In the 1970s and 1980s, limited studies were published in the field of quadratic magneto-optical spectroscopy on bulk YIG crystals, demonstrating magnetic linear birefringence [34] or dichroism [35,36] of YIG doped by rare earths and metals, as well as a sizable Voigt effect in terbium-gallium garnet at cryogenic temperature [37]. However, only few experiments aiming at understanding the details of the quadratic MO response in thin films of pure, undoped YIG have been performed so far.

In this paper, we report on the observation of a giant Cotton-Mouton effect of a 50 nm thin epitaxial film of pure YIG, which can even exceed the amplitude of the linear Faraday effect owing to its origin in ferrimagnetic order of electronic spins. Using a combined experimental and theoretical approach, we quantify the size of CME-induced polarization rotation with respect to various external parameters, such as wavelength, temperature, or angle of incidence. This is a key prerequisite for the quadratic magneto-optics optimization for magnetometric applications. The potential of CME for magnetometry is demonstrated on identification of magnetic anisotropy of the thin YIG film directly from the detected MO signals.

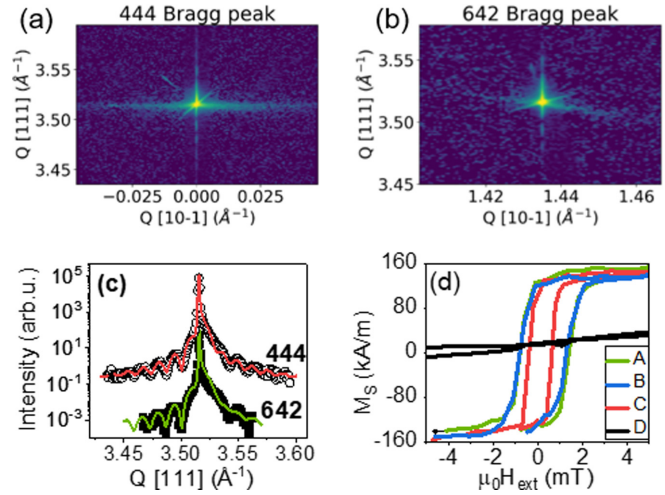

FIG. 1. Structural and magnetic characterization of thin YIG film. (a,b) Reciprocal space maps (RSMs) taken on 444 and 642 Bragg peaks of YIG at room temperature. (c) Cross sections of RSMs data along the [111] crystallographic directions (points) modeled by dynamical diffraction model (line) with lattice parameter $a = 12.379$ Å and distortion angle $\alpha = (90.05 \pm 0.02)^\circ$. (d) Magnetic hysteresis loops measured by SQUID magnetometry in three in-plane crystallographic directions that are denoted as follows: *A* [2 -1 -1], *B*[0 1 -1], and *C* (diagonal), and in the out-of-plane direction *D* [111] at a temperature of 50 K.

II. EXPERIMENTAL DETAILS AND SAMPLE CHARACTERIZATION

We used a monocrystalline 50 nm thick film of yttrium iron garnet prepared by pulsed laser deposition (PLD) on (111)-oriented gallium-gadolinium garnet (GGG). Details of the growth procedure can be found in Ref. [38]. Since the thin YIG layers are prone to growth defects and strain inhomogeneities [14,16], the samples were carefully characterized by x-ray diffraction. From the reciprocal space maps (RSMs) around the YIG and GGG 444 and 642 Bragg peaks we find that any diffraction signal of the film is aligned with that of the substrate along the in-plane momentum transfer [see Figs. 1(a) and 1(b)]. The RSMs thus show the pseudomorphic growth of the YIG film. Its in-plane lattice parameter, equal to the substrate lattice parameter, is measured to be 12.385 Å, close to the previously published values for GGG substrates [39]. Along the [111] direction we find Laue thickness oscillations indicating the high crystalline quality of the YIG film. In order to analyze the out of plane lattice parameter, a cross section along the [111] direction was extracted from the 444 and 642 Bragg peaks and modeled using a dynamical diffraction model [see Fig. 1(c)]. We used the rhombohedrally distorted cubic structure of YIG with $a = 12.379$ Å and rhombohedral angle $\alpha = (90.05 \pm 0.02)^\circ$ as an input for the model, parameters that are similar to Ref. [14]. A weak in-plane tensile strain occurs due to the lattice mismatch, but the resulting distortion of only 0.05 ° is unlikely to affect the magnetic properties of the layer in a significant way.

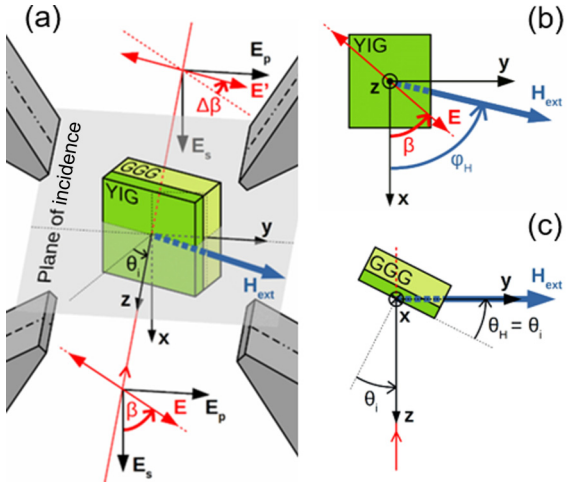

FIG. 2. (a) Schematics of the experimental setup for magneto-optical magnetometry. Linearly polarized light with a polarization $\boldsymbol{E}$ oriented at an angle β with respect to the TE polarization mode ($\boldsymbol{E}_s$) is incident on the sample, which is oriented under an angle θ_i. with respect to the plane in which the magnetic field was applied. After being transmitted through the sample, the light polarization plane is rotated by an angle $\Delta\beta$. The sample is subject to an external magnetic field $\boldsymbol{H}_{\text{ext}}$, applied in an arbitrary direction, with the corresponding spherical angles of the $\boldsymbol{H}_{\text{ext}}$ vector shown in (b) plane view projection (azimuthal angle φ_H) and (c) side view projection (polar angle θ_H) of the experimental geometry.

Magnetic properties of the YIG film were studied using SQUID magnetometry. An example of hysteresis loops recorded at 50 K with external magnetic field applied along different crystallographic directions is shown in Fig. 1(d). Clearly, the sample is in-plane magnetized, with a coercive field of $\mu_0 H_c = 1.8$ mT. Note that there is a small difference in H_c between the two crystallographic directions denoted as A and C, indicating the presence of an in-plane magnetic anisotropy. However, its quantification based on our SQUID measurement is prevented by a large error caused by the paramagnetic background of the GGG substrate. For further details on SQUID see Sec. 1 in the Supplemental Material [40] (also see Refs. [41,42]). From the SQUID data, the room-temperature value $M_s = 96$ kA/m was extracted. The saturation magnetization is lower than that of a bulk crystal $M_{\text{s,bulk}} = 143$ kA/m [43] but in very good agreement with previously reported values for PLD-grown ultrathin YIG layers [17], confirming the good quality of our YIG film.

Magneto-optical measurements on the YIG sample were performed by a homemade vector magneto-optical magnetometer, schematically shown in Fig. 2(a). For the majority of our experiments we used a cw solid-state laser (Match Box series, Integrated Optics Ltd.) with a fixed wavelength of 403 nm as a light source. The cw laser was replaced by the second-harmonics output of a tunable titan-sapphire pulsed laser (model Mai Tai, Spectra Physics) to gain a wider spectral range of $\lambda = 390$–440 nm for the wavelength-dependent measurement. The light was incident on the sample either under an angle $\theta_i = 3^\circ$ (near normal incidence), or $\theta_i = 45^\circ$, as indicated in Fig. 2(c). Linear polarization of the incident light was set by a polarizer and a half-wave plate. In both cases, the polarization state of the light transmitted through the sample was analyzed by a differential detection scheme (optical bridge) in combination with phase-sensitive (lock-in) detection [44].

The sample itself was mounted in a closed-cycle cryostat (ARS Systems) to enable the temperature variation in a range of $T = 20$ K–300 K. The cryostat was placed between pole stages of a custom-made two-dimensional (2D) electromagnet where the external magnetic field of up to $\mu_0 H_{\text{ext}} = 205$ mT could be applied in an arbitrary direction in the plane perpendicular to the optical beam axis. The (spherical) coordinate system for $\boldsymbol{H}_{\text{ext}}$ is given in Figs. 2(b) and 2(c). Note that the polar angle θ_H is defined from the sample plane, and it is equivalent to the angle of incidence of the incoming light θ_i. Utilization of the 2D electromagnet allowed for two different approaches in our experiments. Firstly, a standard magneto-optical magnetometry was used, where the magnitude of $|\boldsymbol{H}_{\text{ext}}|$ in a fixed y direction is varied, and the resulting hysteresis loops are recorded. Comparing the measured hysteresis loops for different orientations of the light polarization with our analytical model allowed for determination of the magnetization reorientation during the magnetic field sweeps, as further discussed in Sec. III, Theory. Analysis of the full polarization dependence of the hysteresis loops also enabled us to separate the contributions of LMET (linear in magnetization) and CME (quadratic in magnetization) to the overall MO signals, and to extract their corresponding amplitudes.

However, this method of determining the size of the MO effects was inefficient and burdened by a relatively large error resulting from the complicated separation of the MO effects that required full light polarization dependence of the hysteresis loops. Therefore, for further systematic study of the CME we implemented the Magnetic Optic Kerr Effect with a rotating field (ROT-MOKE) experiment, where the external magnetic field of a fixed magnitude of 205 mT was rotated in the sample plane, the azimuthal angle ranging from $\varphi_H = 0^\circ$ to 360° (see Fig. 2). The resulting MO signal was recorded as a function of φ_H [24,25], with the polarization of light kept fixed to the fundamental TE (s-) mode. In these experiments, H_{ext} was large enough to saturate the magnetization of the YIG film, which then exactly followed the field direction during its rotation. We can therefore neglect the effect of magnetic anisotropy and determine the MO coefficient simply from one field rotation curve [25], in a way very similarly to determination of AMR or planar Hall effect coefficients from field rotations [26]. This also directly demonstrates the analogy between magneto-optical and magnetotransport methods.

III. THEORY

The aim of our theoretical analysis is to determine the kinetics of the magnetization vector during the magnetic field sweep and to evaluate the magnitude of the magneto-optical coefficient. Reorientation of the magnetization vector is modeled in terms of the local profile of the magnetization free energy density. Its functional F is known from the symmetry considerations (see Eq. (S1) in the Supplemental Material [40]) assuming the lowest terms in magnetization magnitude [45], yet the corresponding constants, which appear in the expression, are strongly sample dependent. In bulk YIG

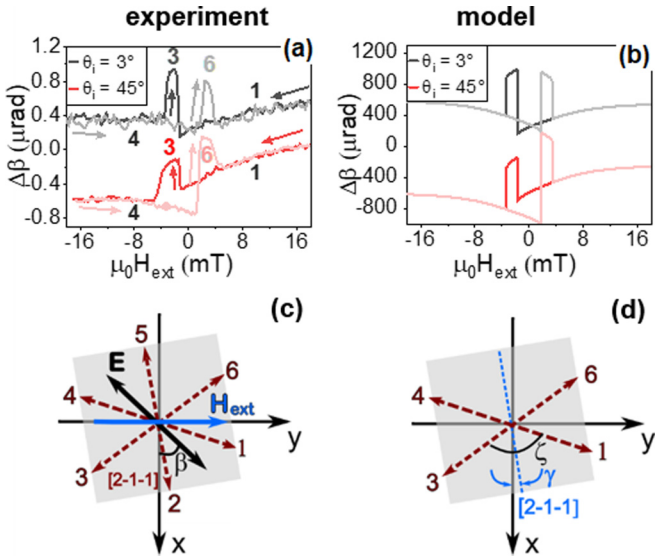

FIG. 3. (a) Rotation of polarization plane $\Delta\beta$ as a function of the external magnetic field magnitude $\boldsymbol{H}_{\text{ext}}$ measured for two angles of incidence, $\theta_i = 3^\circ$ and 45°, corresponding to the same two field angles, $\theta_H = 3^\circ$ and 45°, respectively; a temperature of 20 K and photon energy of 3.1 eV was used. The data were vertically shifted for clarity. The complex M-shape-like hysteresis is a clear signature of magnetization being switched between magnetic easy axes. (b) Simulation of the MO signal by means of the analytical model. Based on our model, we identified three equivalent easy axes (c) and extracted their mutual angle $\zeta = 120^\circ$ and position of their bisectrix $\gamma = 6^\circ$. (d) The abrupt changes in magneto-optical signals in (a,b) correspond to "jumps" of magnetization between the easy axes 1, 3, and 4 (4, 6, and 1) for the magnetic field sweep from the positive (negative) field, as schematically indicated in (a).

crystal the anisotropy constants are known [46] and, therefore, we can roughly estimate the positions of the easy magnetization directions. The dominant anisotropy in a high-quality thin YIG layer on GGG is the cubic bulk contribution. In thin samples, there is an additional out of plane anisotropy (hard direction) due to the stress fields and demagnetization energy which pushes the magnetization towards the sample plane [14,15]. We therefore expect that the projection of easy directions to the [111] crystallographically oriented sample plane is effectively sixfold [see Fig. 3(c)]. The deflection angle of the easy directions from the sample plane is only a few degrees and thus can be neglected (see Sec. 3 in the Supplemental Material [40] for more details). We define an effective in-plane anisotropic energy density with the corresponding sixfold symmetry as

$$F = K_6 \sin^2 3(\varphi_M - \gamma) - M_s \mu_0 H_{\text{ext}} \cos\theta_H \cos(\varphi_H - \varphi_{\text{M}}), \tag{1}$$

where M_S is the saturation magnetization of the sample, μ_0 is the vacuum permeability, H_{ext} is the external magnetic field magnitude, θ_H its deflection angle from the sample plane, and φ_H its azimuthal orientation. The symbol φ_M denotes the azimuthal angle of the in-plane magnetization vector and K_6 is the effective anisotropy constant. The symbol γ represents a rotation angle of an easy axis closest to the x direction, resulting from an unintentional rotation of the sample in the experiment [see Figs. 2, 3(c), and 3(d) for the coordinate system]. It also describes the orientation of the bisectrix between the two easy directions, involved in the magnetization switching process that was utilized for evaluation of the MO coefficients

When interpreting the experimental data, we simulated the full magneto-optical measurement of the hysteresis by calculating the MO response of the layered structure (50 nm thick sample on a 500 μm thick substrate) using Yeh's formalism [47]. Our calculations inherently include all multiple reflections and resulting interferences. As such, they reveal the sum of all MO effects which take part in the particular geometry.

In our calculations, we consider the refractive index of the thick GGG substrate to be $n_S = 1.96$. The YIG permittivity tensor for magnetization oriented along the x axis is defined as [48]

$$\epsilon(\varphi_M = 0) = \begin{pmatrix} \epsilon^{(0)} & 0 & 0 \\ 0 & \epsilon^{(0)} - 2M_S^2 G_A & M_S K \\ 0 & -M_S K & \epsilon^{(0)} - 2M_S^2 G_A \end{pmatrix}. \tag{2}$$

We take the permittivity of the material as $\epsilon^{(0)} = 6.5 + 3.4i$ [49], $M_S K$ is the component of the isotropic magneto-optical K tensor, $M_S^2 G_A = (G_{1111} - G_{1122})/2$ is a combination of the particular components of the G tensor, and $\boldsymbol{M}_S$ is the saturation magnetization. For more details see Sec. 4 of the Supplemental Material [40].

Owing to the cubic symmetry of the YIG crystal, its permittivity tensor for an arbitrary magnetization orientation in the sample's xy plane is calculated by a proper rotation of the tensor in Eq. (2) around the z axis, corresponding to the [111] crystallographic direction. The values of the magneto-optical components of the permittivity tensor were chosen to best fit our experimental data, as discussed later in this section.

Besides the fundamental wave-optics approach, the experimental data can be interpreted also in terms of the symmetry of the MO response. The signals are composed of components even and odd in magnetization, respectively. The even contribution is related to the Cotton-Mouton effect and is represented by the parameter $M_S^2 G_A$ in Eq. (2), which is quadratic in magnetization. The odd contribution can be phenomenologically understood as a combination of the longitudinal and transverse linear magneto-optical effects, and it is described by the parameter $M_S K$ in Eq. (2), linear in magnetization. Note also that the polar Faraday effect does not contribute to the overall MO response of the system because the projection of magnetization to the polar (out of plane) direction is negligible.

According to the calculations presented in Sec. 5 of the Supplemental Material [40], polarization rotation due to LMET may be expressed in the major terms as

$$\Delta\beta_{\text{LMET}}(\varphi_{\text{M}}, \beta) = \left[P_0^{\text{LMET}} + P^{\text{LMET}} \cos 2\beta\right] \sin\varphi_{\text{M}}, \tag{3}$$

where we defined the effective LMET coefficients P^{LMET} and P_0^{LMET} for the polarization-dependent and -independent parts, respectively. In contrast to the linear MO effect [Eq. (3)], the quadratic CME is sensitive to the angle between the magnetization and light polarization directions. A simple relation can be derived, describing the relation between polarization rotation $\Delta\beta_{\text{CME}}$ and magnetization

position φ_M [23]:

$$\Delta\beta_{\mathrm{CME}}(\beta, \varphi_M) = P^{\mathrm{CME}} \sin 2(\varphi_M - \beta), \tag{4}$$

where we defined the effective CME coefficient P^{CME}, which is connected with the quadratic permittivity tensor components.

IV. EXPERIMENTAL RESULTS

A. Hysteresis loops

Firstly, we focused on studying the MO signal during external magnetic field sweeps (MO hysteresis loops in the following). In Fig. 3(a) we show an example of the MO hysteresis loop measured close to the normal incidence ($\theta_i = 3^\circ$) and at a large angle of incidence ($\theta_i = 45^\circ$) at 20 K. The character of the hysteresis loops changes significantly when deviating from the normal incidence. Close to the normal incidence, the signal displays an M-shape-like loop, typical for the quadratic MO effects [44]. The steps in the M-shape loops generally correspond to a switching of magnetization between two magnetic easy axes [44]. In contrast, the hysteresis loop gains a more complex shape for $\theta_i = 45^\circ$. Besides the M-shape-like signal, which is still present with virtually unchanged size, there is another squarelike component that indicates the presence of a signal odd in magnetization, which can be attributed to LMET.

In order to understand the nature of the magnetization dynamics, we used the theoretical approach described in the Theory section to model the observed signals: We consider six effective in-plane easy directions for magnetization [see Eq. (1)] and we numerically modeled the MO response considering the parameters of the experiment. We used four fitting parameters: Two of them are related to the amplitude of the MO effects (even and odd) and two describe the magnetic anisotropy. The best agreement with the experimental data appears for the values of $M_S K = 0.058\exp[0.46i]$ and $M_S^2 G_{\mathrm{A}} = M_S^2(G_{1111} - G_{1122})/2 = 0.0035\exp[-1.05i]$, $\gamma = 6^\circ$ and $K_6 = 61$ J/m^3 (for more information about the fitting procedure see Sec. 4 of the Supplemental Material [40]). As an output of our model, the correct shape of the MO loops is obtained, as shown in Fig. 3(b).

The magnetic anisotropy utilized by the model is schematically depicted in Fig. 3(c), with a definition of the magnetic easy axes position given in Fig. 3(d). Note that the estimated magnetic anisotropy agrees with the SQUID measurement [Fig. 1(d)], the diagonal orientation ("*C*") being the closest to the position of one of the easy axes. The reorientation of the magnetization vector $\boldsymbol{M}$ in the external magnetic field gained from our model is schematically indicated in Fig. 3(a). For the large positive external field $\boldsymbol{H}_{\mathrm{ext}}$, $\boldsymbol{M}$ is oriented along the field direction, close to the easy axis (EA) labeled as "1." While decreasing $\boldsymbol{H}_{\mathrm{ext}}$, $\boldsymbol{M}$ is slowly rotated towards the direction of EA "1." When $\boldsymbol{H}_{\mathrm{ext}}$ of the opposite polarity and magnitude exceeding the value of coercive field H_c is applied, $\boldsymbol{M}$ switches directly to the EA "3" by rotating by ∼120°. Further increase of the negative $\boldsymbol{H}_{\mathrm{ext}}$ leads to another switching, this time by 60 ° to EA "4," until, finally, $\boldsymbol{M}$ is again oriented in the direction of $\boldsymbol{H}_{\mathrm{ext}}$. A symmetrical process takes place in the second branch of the hysteresis loop. Note that the same magnetization switching occurs independently of the angle of incidence, though for larger θ_i the shape of the loop is distorted by the presence of the MO signal linear in magnetization.

The macrospin simulations confirmed that the full magnetization trajectory extracted from our magneto-optical signals corresponds to the realistic magnetic anisotropy constants for thin YIG films (see Sec. 3 of the Supplemental Material [40]). The model allows for certain ambiguity in its parameters since we do not have access to the out of plane components of magnetization reorientation during the switching, to compare them with the experimental data. The model thus cannot be used reliably for obtaining all magnetic anisotropy constants of the material without the support of a complementary experimental method. However, it provides a useful tool for prediction of the behavior of the magneto-optical effects, as shall be shown further on.

In order to quantify the contributions of the linear and quadratic MO effect, we recorded the MO hysteresis loops for different angles β of incident light polarization. Contributions to the MO signals that are linear (LMET) and quadratic (CME) in magnetization were obtained by antisymmetrization and symmetrization of the hysteresis loops, respectively. The data separation can be done in the following way.

In general, we measure the polarization rotation change upon magnetization reorientation in our experiment. Therefore, we define the LMET amplitude A^{LMET} as

$$\begin{aligned} A^{\mathrm{LMET}}(\varphi_1, \varphi_2) &= P^{\mathrm{LMET}}(\sin\varphi_1 - \sin\varphi_2) \\ &= \tfrac{1}{2}[\Delta\beta(\varphi_1) - \Delta\beta(\varphi_2)] \\ &\quad - \tfrac{1}{2}[\Delta\beta(\varphi_1 + 180^\circ) - \Delta\beta(\varphi_2 + 180^\circ)], \end{aligned} \tag{5}$$

where $\Delta\beta$ is the polarization rotation (including all magneto-optical and nonmagnetic contributions) for a given orientation of magnetization $\boldsymbol{M}$; φ_1 and φ_2 are the two positions of $\boldsymbol{M}$ in the magnetization reorientation process. The difference in each of the square brackets represents the experimentally measured change of the MO signal when the position of $\boldsymbol{M}$ changes between φ_1 and φ_2. The subtraction of the parentheses then corresponds to the data antisymmetrization; i.e., it extracts only the linear (odd) LMET component from the MO signal.

Equivalently, we may define the CME amplitude (see Fig. 4 and Eq. (11) in Ref. [44]) as

$$\begin{aligned} A^{\mathrm{CME}}(\beta, \varphi_1, \varphi_2) &= 2P^{\mathrm{CME}} \sin\xi \cos 2(\gamma - \beta) \\ &= \tfrac{1}{2}[\Delta\beta(\varphi_1) - \Delta\beta(\varphi_2)] \\ &\quad + \tfrac{1}{2}[\Delta\beta(\varphi_1 + 180^\circ) - \Delta\beta(\varphi_2 + 180^\circ)], \end{aligned} \tag{6}$$

where $\xi = \varphi_1 - \varphi_2$ is the angle between the easy axes and $\gamma = (\varphi_1 + \varphi_2)/2$ is the position of their bisectrix. The right-hand side of the equation represents the symmetrization of the MO signal.

Knowing the angles $\varphi_{1,2}$ from the hysteresis loop modeling, it is possible to extract the MO coefficients using the above expressions.

The corresponding symmetrized and antisymmetrized components of the MO field-sweep loops are depicted in Figs. 4(a) and 4(b) for the two angles of incidence $\theta_i = 3^\circ$

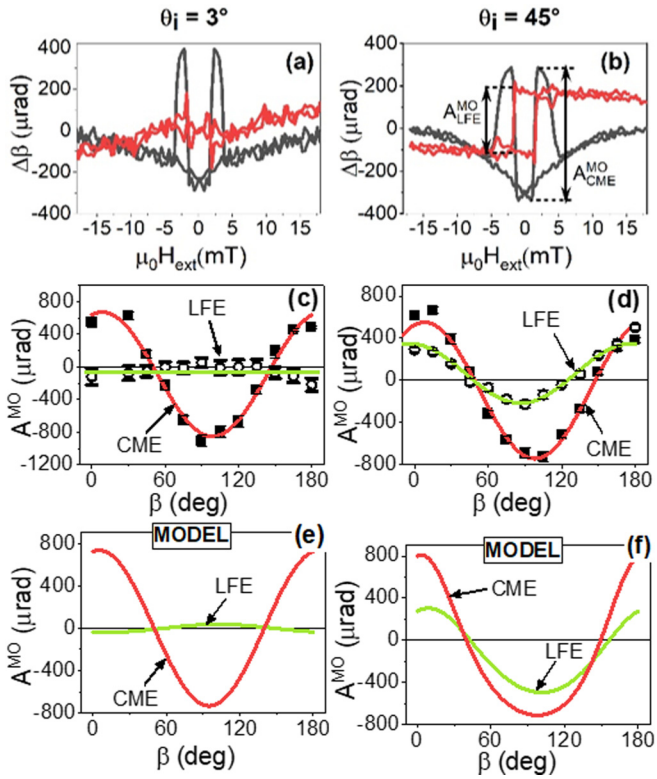

FIG. 4. Analysis of magneto-optical signals at an angle of incidence $\theta_i = 3^\circ$ (left column) and $\theta_i = 45^\circ$ (right column). For extracting the MO effects odd and even in magnetization, the signals were decomposed to antisymmetric (red line) and symmetric (black line) components with respect to $\boldsymbol{H}_{\text{ext}}$. An example of results of this procedure is shown for MO signals measured using $\beta = 0^\circ$ for angles of incidence (external field) $\theta_H = \theta_i = 3^\circ$ (a) and $\theta_H = \theta_i = 45^\circ$ (b); the original data are shown in Fig. 3(a). The amplitudes of A^{LMET} and A^{CME} for each polarization angle β were determined from the size of the "jumps" in hysteresis loops, as indicated in (b).

and 45°, respectively. Note that after the separation, the signal indeed splits into the square-shape hysteresis loop typical for the linear MO effect, and the characteristic M-shape loop of the quadratic MO effect.

The polarization dependencies of LMET and CME for $\theta_i = 3^\circ$ (c) and $\theta_i = 45^\circ$ are shown in Fig. 4(d). Points stand for the measured data. The green line corresponds to the fit by Eqs. (3) and (5), with amplitude $P^{\text{LMET}} = (280 \pm 20)$ μrad, assuming that the switching takes place between the easy axes separated by 120°. The red line is the fit by Eq. (6), where $P^{\text{CME}} = (450 \pm 30)$ μrad for $\theta_i = 3^\circ$, and $P^{\text{CME}} = (320 \pm 20)$ μrad for $\theta_i = 45^\circ$. Comparison with the analytical model for the polarization dependence of MO signals for $\theta_i = 3^\circ$ [Fig. 4(e)] and $\theta_i = 45^\circ$ [Fig. 4(f)] shows excellent agreement, confirming the validity of our model.

For further analysis, we need to determine the amplitudes of the MO effects attributed to the particular magnetization switching process according to Eqs. (5) and (6). The amplitude of the even component A^{CME} is taken from the first $\zeta = 120^\circ$ magnetization switching, as indicated in Fig. 4(b). The amplitude of the odd component A^{LMET} is obtained from the same 120° switching, i.e., $\varphi_1 = -\varphi_2 = 60^\circ$ in Eq. (5). This method also eliminates potential contributions from the paramagnetic GGG substrate, where no steplike hysteretic behavior is expected.

The resulting amplitudes of the separated MO signals are shown as a function of the light polarization in Figs. 4(c) and 4(d) for the angles of $\theta_i = 3^\circ$ and 45°, respectively. Points in the graphs indicate the values extracted from the experiments, lines are fits by Eqs. (3) and (6), from which the values of the effective MO coefficients $P^{\text{CME}} = (320 \pm 20)$ μrad and $P^{\text{LMET}} = (280 \pm 20)$ μrad were extracted for the 45° incidence angle, and $P^{\text{CME}} = (450 \pm 30)$ μrad for the near-normal incidence. Note that even for $\theta_i = 45^\circ$, which is optimal for observation of the LMET, the strength of the quadratic CME exceeds that of the linear LMET, and reaches values comparable to other systems well known for strong quadratic magneto-optics [27,28].

The observed polarization dependence of MO signal amplitudes can be better understood in terms of our analytical model. Keeping all the input parameters of the model fixed, we calculated polarization dependencies of the individual MO amplitudes extracted from the modeled MO hysteresis loops. The resulting dependencies are presented Figs. 4(e) and 4(f) for $\theta_i = 3^\circ$ and 45°, respectively. The theoretical curves follow the experimental data very well even for the LMET signal close to the normal incidence, which indicates the validity of our analytical approach. We can therefore extend the predictions of the model to conditions that are not easy to change systematically in experiments, particularly the dependence on the incidence angle and the sample thickness.

In Fig. 5 we illustrate these dependencies separately for CME (graphs in the left column) and LMET (right column). The material parameters for each curve are set separately such that $P^{\text{CME}} = 450$ μrad at near-normal incidence, keeping the phase of the parameter $M_S^2 G_A$ equal to −1.05, which best fits the data. The parameter $P^{\text{LMET}} = 280$ μrad is taken for the 45° angle of incidence, provided that $A^{\text{LMET}}(\beta = 0) = 310$ μrad. This procedure is chosen to highlight differences in the CME and LMET in terms of their polarization dependence, which is crucial for analyzing magnetometry signals [23,27]. In reality, amplitudes of both LMET and CME would scale with the sample thickness in a nontrivial way.

We used a simplified scheme to model the data, considering only the 120° magnetization reorientation for CME and LMET. Remarkably, there is a significant difference in how the polarization dependence of the linear and the quadratic MO effect is affected by changing both the sample thickness and the angle of incidence. Nonintuitively, the polarization dependence of CME is only weakly affected by both these parameters. Its shape is slightly modified for large angles of incidence θ_i [Fig. 5(a)] and, similarly, the sample thickness has almost no effect on the shape of the CME signals [Fig. 5(c)]. In contrast, the linear MO signals are drastically modified by both these parameters. As expected, the linear MO effect decreases for smaller angles of incidence [Fig. 5(b)], eventually disappearing at normal incidence. However, not only the magnitude but also the shape of the polarization dependence is affected. This complex behavior of LMET results from optical interferences: The most general argument relies on the symmetry. When considering magnetization oriented in the sample plane, this plane becomes the plane of symmetry of the YIG permittivity in the

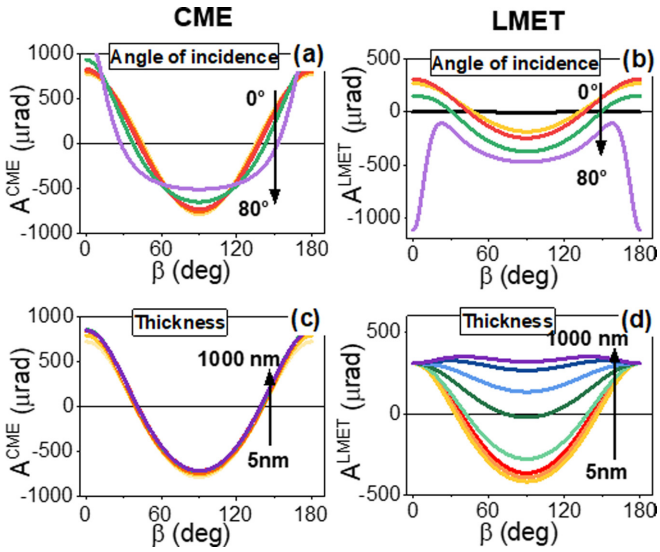

FIG. 5. Amplitudes of CME (left column) and LMET (right column) as a function of incident polarization angle β, extracted from the hysteresis loops obtained from the analytical model. The amplitudes A^{CME} and A^{LMET} are obtained by the same method as in Fig. 4. Polarization dependence of (a) CME and (b) LMET effects for various angles of incidence θ_i and fixed sample thickness of 50 nm. The angles of incidence of $\theta_i = 0°$, 30°, 40°, 60°, and 80° are shown; the arrow indicates increase of θ_i. Clearly, the LMET is very strongly angle dependent, while CME is much less affected. The same feature can be observed for changing the sample thickness d. While the polarization dependence of CME (c) does not depend on the sample thickness, LMET (d) can vary significantly. The thicknesses of $d = 5, 10, 20, 50, 100, 200, 500$, and 1000 nm are displayed for the angle of incidence $\theta_i = 45°$.

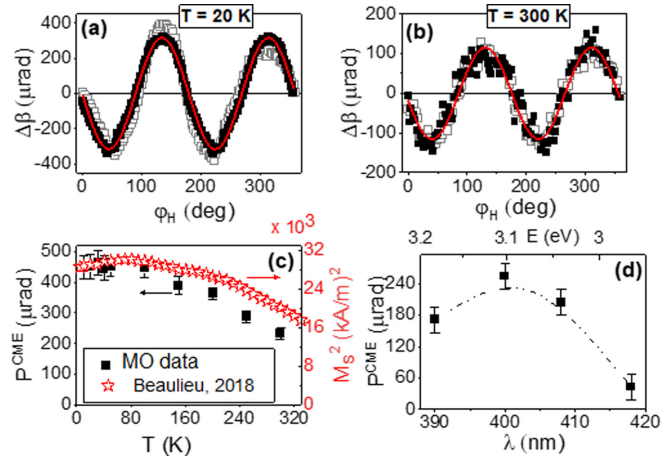

FIG. 6. Rotation of polarization plane $\Delta\beta$ as a function of the direction φ_H of the external magnetic field of a fixed magnitude $\mu_0 H_{\mathrm{ext}} = 205$ mT, measured at 20 K (a) and at room temperature (b). Polarization was set to $\beta = 0°$. Open squares indicate the as-measured data; full squares are symmetrized in φ_H to remove linear magneto-optical effects. The red line is a fit to Eq. (4) for $\varphi_H = \varphi_M$ as $\boldsymbol{H}_{\mathrm{ext}}$ is large enough to saturate magnetization of the sample. Magneto-optical coefficients for the Cotton-Mouton effect obtained from the fits are $P^{\mathrm{CME}} = 450$ μrad at 20 K and $P^{\mathrm{CME}} = 230$ μrad at 300 K. (c) The decrease of P^{CME} with increasing temperature is well correlated with the reduction of the square of the saturation magnetization M_S^2, values of which were taken from Ref. [50] (and converted to SI units). (d) The spectral dependence of P^{CME} measured at room temperature (d) clearly shows a peak at around 3.1 eV.

case of nonzero quadratic MO interaction and zero linear MO interaction. If, however, there are nonzero linear MO terms, then it is not the plane of symmetry of the permittivity tensor. In particular, when there are interferences, i.e., interfering light waves traveling forth and back inside the YIG layer, there is a qualitative difference between the linear and quadratic MO response. In the case of the CME effect, waves propagating forth and back undergo the same MO interaction due to the symmetry and the overall result can be understood as a multiplication of a single pass MO response by an effective number of interfering light waves. The linear effect lacks this particular symmetry and is therefore much more sensitive to interferences as seen in Figs. 5(b) and 5(d). This complex modification of the LMET response makes it difficult to optimize the sample thickness for magnetometry measurements. Therefore, using the quadratic CME for this purpose provides a significant advantage.

It is important to stress that our model is independent of the magnetic anisotropy of the particular sample. The conclusions drawn from the model are, therefore, universal for a series of samples with identical bulk magnetic properties.

B. ROT MOKE measurements

In order to further investigate the nature of the Cotton-Mouton effect, we performed ROT MOKE measurements [24,25] in near-normal incidence geometry to eliminate the linear MO contribution to the signal. The ROT MOKE method provides a more efficient and sensitive tool for extracting the MO coefficients, without the necessity of changing the incident light polarization orientation.

Examples of the as-measured ROT MOKE signals are shown as open symbols in Figs. 6(a) and 6(b) for low temperature ($T = 20$ K) and room temperature, respectively. Since we are interested in even MO signals only, the small contribution of linear MO effect was removed from the data by symmetrization with respect to the angle of the external field φ_H. The symmetrized curves [solid symbols in Figs. 6(a) and 6(b)] display a clear harmonic behavior, which indicates that the external field of 205 mT was large enough to saturate magnetization, which follows exactly the direction φ_H. This allowed us to fit the data directly to Eq. (4) (red line), with the angle of magnetization equal to the angle of $\boldsymbol{H}_{\mathrm{ext}}$ ($\varphi_H = \varphi_M$). From the fits we obtain the MO coefficient $P^{\mathrm{CME}} = (450 \pm 40)$ μrad at 20 K, which is in excellent agreement with the value extracted from the hysteresis loops. The value of the CME coefficient decreases to $P^{\mathrm{CME}} = (230 \pm 20)$ μrad when heating the sample to room temperature. To understand this change, we evaluated the P^{CME} coefficient in a relatively large temperature range. Generally, since the CME is of the second order in magnetization, scaling of P^{CME} with the square of saturation magnetization M_s is expected [22,32]. As illustrated in Fig. 6(c), the good correlation between these two quantities confirms the intrinsic magnetic origin of the CME effect, as further elaborated upon in the Supplemental Material [40] and Fig. S2 therein. Note that the imperfect matching between

P^{CME} and M_S^2 suggests a presence from "extrinsic" contributions to P^{CME}, which include, for example, a cooling-induced strain and the resulting modification of the optical and/or magneto-optical properties of the material.

The physical origin of the intrinsic CME effect can be unveiled by its spectral dependence. For this purpose, we extracted the P^{CME} coefficient from the room-temperature data, measured at several wavelengths. The obtained spectrum of P^{CME} is presented in Fig. 6(d). The maximum of CME occurs at around $\lambda = 400$ nm (3.1 eV), and its amplitude drops rapidly when the laser is detuned from the central wavelength by more than 10 nm. The sharp increase of the CME response around 3.05–3.1 eV corresponds energetically to transitions O-2p to Fe-3d band states of YIG [51]. A giant Zeeman shift of this transition level was recently reported in a 50 nm thin [111] YIG film [51], which is very similar to the sample studied in our work. Its origin was attributed to the combination of strong exchange interaction of Fe-3d orbitals and the effect of spin-orbit coupling on the Fe-3d bands. A similar combined act of the exchange of magnetic ions and spin-orbit coupled valence bands is known from diluted magnetic semiconductors [28,52], the systems that are typical for their strong quadratic MO response with a significant peak on the Zeeman-split energy level [52]. Analogically, a strong quadratic response of the YIG thin layers at this spectral range can be expected [52].

V. DISCUSSION

The microscopic explanation of the large CME effect compared to the linear MO effect of YIG relies on the ferrimagnetic order of the magnetic moments. As discussed in a recent theoretical work [52], the macroscopic net magnetic moment of YIG is a sum of contributions from two sublattices formed by Fe ions at tetragonal and octahedral symmetry positions, respectively. Since the sublattices are coupled antiferromagnetically, magnetic momenta of the sublattices subtract. Nonzero net magnetic moment is present due to a larger number of Fe ions in tetragonal positions within the YIG unit cell. The crystal field splits Fe-3d orbitals of both symmetries to e_g and t_{2g} symmetry states [53] in such a way that the linear MO response of each of the sublattices, which is given by the transition from Zeeman-split O-3p valence orbitals, has an opposite sign. Therefore, the macroscopic linear MO response is diminished. In contrast, the quadratic MO response from the two respective sublattices is additive, and is not weakened by their antiferromagnetic orientation. Although the quadratic MO response is roughly of the same order as that observed, for example, in Heusler alloys [27], the ratio of the quadratic/linear amplitudes (R_Q/R_L) significantly exceeds 1, while the maximum value observed in Co_2FeSi is only about $R_Q/R_L = 0.7$ [27]. Even in EuO-based ferromagnetic semiconductors, where record values of quadratic MO response (up to $R_Q = 4$ mrad at cryogenic temperatures) have been reported recently [54], this ratio does not exceed $R_Q/R_L = 0.6$; the linear MO effect still significantly exceeds the quadratic MO response.

Apart from the intrinsic MO effect, impurity states can significantly influence the MO response of thin films. Lattice defects are known to occur during growth of the very thin YIG layers, particularly due to the migration of Fe^{3+} and Gd^{3+} ions across the interface during the postgrowth annealing [14,15,18]. Similarly, gadolinium doping can be responsible for the decrease in saturation magnetization of the PLD-grown thin YIG layers [17]. However, it mostly affects the interfacial layer with a thickness of a few nanometers, which orders antiferromagnetically, reducing the magneto-optical response of the layer [55], and cannot thus be responsible for the origin of the observed Cotton-Mouton effect. In fact, previous works based on the quadratic MO response of YIG [20,21] were always performed in a spectral region close to 400 nm, even though thin films of various thickness, prepared by different methods and presumably containing different level of impurities, were studied. Though the choice of the wavelength was not performed systematically in these works and the amplitude of CME was not evaluated, the wavelengths were always close to the optimum value identified in our experiments. We are thus led to the conclusion that the observed strong CME response is very likely intrinsic to any YIG thin layer, and it is not related to unintentional doping or any type of defects. Unlike in most of the other materials researched by quadratic magneto-optics [28,54], the strong Cotton-Mouton effect in YIG occurs even at room temperature. Therefore, the quadratic magneto-optics seems to be universally applicable for sensitive magnetometry measurements in this material.

VI. CONCLUSIONS

In summary, we have shown the presence of a strong Cotton-Mouton effect in a 50 nm thick epitaxial layer of YIG in the spectral region close to 400 nm. We measured both magneto-optical hysteresis loops and ROT MOKE data that enabled us to extract the values of the CME magneto-optical coefficient and to determine the magnetocrystalline anisotropy of the studied thin YIG film. The maximum value ($P^{\mathrm{CME}} = 450$ μrad) obtained for our YIG layer exceeds the linear MO response amplitude in this material. Importantly, CME is rather strong even at room temperature, which make it a useful tool for optospintronic and magnetometric experiments. Both spectral and temperature dependences indicate an intrinsic origin of CME, which we attributed to specific ferrimagnetic transitions (O-3p to Fe-3d) where the MO response linear in magnetization subtracts for the two sublattices, while the MO signal quadratic in magnetization adds up constructively.

The measured signals were analyzed in detail using a theoretical model based on a calculation of the overall optical and magneto-optical response of the thin YIG layer on a GGG substrate. The model enables us to predict properties of the Cotton-Mouton effect and the linear magneto-optical effect in transmission for variable sample thicknesses and angles of incidence, which is crucial for many thin-film experiments. The calculation revealed that while LMET varies strongly both with angle of incidence and sample thickness, CME has a comparable magnitude but much weaker sensitivity to both of these parameters. Therefore, using CME provides an advantage against LMET, particularly when the normal light incidence is dictated by the experiment geometry, which is the case for most of the optospintronics experiments. Our combined theoretical and experimental approach enables us to

optimize the conditions for the experiment in terms of choice of proper light source and/or measurement geometry, which can lead to a significant increase in signal to noise ratio and sensitivity in the optospintronics experiments.

ACKNOWLEDGMENTS

The authors would like to acknowledge fruitful discussions with Dr. Jaroslav Hamrle and Dr. Eva Jakubisová. This work was supported in part by the MEYS CR, program INTER-COST, Grant No. LTC20026 and by the EU FET Open RIA Grant No. 766566. We also acknowledge Czech-NanoLab Project No. LM2018110 funded by MEYS CR for the financial support of the measurements at LNSM Research Infrastructure as well as the Deutsche Forschungsgemeinschaft (projects A01 and B02/268565370, SFB TRR173 Spin+X).

E.S. and T.O. contributed equally to the work.

[1] M. Wu and A. Hoffman, *Recent Advances in Magnetic Insulators—From Spintronics to Microwave Applications*, Solid State Physics Vol. 64 (Elsevier Academic Press, Amsterdam, 2013).

[2] L. J. Cornelissen, J. Liu, R. A. Duine, J. Ben Youssef, and B. J. van Wees, Nat. Phys. **11**, 1022 (2015).

[3] H. Quin, S. J. Hämäläinen, and S. van Dijken, Sci. Rep. **8**, 5755 (2018).

[4] B. Heinz, T. Brächer, M. Schneider, Q. Wang, B. Lägel, A. M. Friedel, D. Breitbach, S. Steinert, T. Meyer, M. Kewenig *et al.*, Nano Lett. **20**, 4220 (2020).

[5] Y. Kajiwara, K. Harii, S. Takahashi, J. Ohe, K. Uchida, M. Mizuguchi, H. Umezawa, H. Kawai, K. Ando, K. Takanashi *et al.*, Nature (London) **464**, 262 (2010).

[6] B. Heinrich, C. Burrowes, E. Montoya, B. Kardasz, E. Girt, Y. Y. Song, Y. Sun, and M. Wu, Phys. Rev. Lett. **107**, 066604 (2011).

[7] S. Klingler, V. Amin, S. Geprägs, K. Ganzhorn, H. Maier-Flaig, M. Althammer, H. Huebl, R. Gross, R. D. McMichael, M. D. Stiles *et al.*, Phys. Rev. Lett. **120**, 127201 (2018).

[8] L. Wang, Z. Lu, J. Xue, P. Shi, Y. Tian, Y. Chen, S. Yan, L. Bai, and M. Harder, Phys. Rev. Appl. **11**, 044060 (2019).

[9] H. Nakayama, M. Althammer, Y.-T. Chen, K. Uchida, Y. Kajiwara, D. Kikuchi, T. Ohtani, S. Geprägs, M. Opel, S. Takahashi *et al.*, Phys. Rev. Lett. **110**, 206601 (2013).

[10] C. Y. Guo, C. H. Wan, W. Q. He, M. K. Zhao, Z. R. Yan, Y. W. Xing, X. Wang, P. Tang, Y. Z. Liu, S. Zhang *et al.*, Nat. Electron. **3**, 304 (2020).

[11] K. Uchida, J. Xiao, H. Adachi, J. Ohe, S. Takahashi, J. Ieda, T. Ota, Y. Kajiwara, H. Umezawa, H. Kawai *et al.*, Nat. Mater. **9**, 894 (2010).

[12] T. Kikkawa, K. Uchida, Y. Shiomi, Z. Qiu, D. Hou, D. Tian, H. Nakayama, X.-F. Jin, and E. Saitoh, Phys. Rev. Lett. **110**, 067207 (2013).

[13] K. S. Olsson, K. An, G. A. Fiete, J. Zhou, L. Shi, and X. Li, Phys. Rev. X **10**, 021029 (2020).

[14] B. Bhoi, B. Kim, Y. Kim, M.-K. Kim, J.-H. Lee, and S.-K. Kim, J. Appl. Phys. **123**, 203902 (2018).

[15] C. T. Wang, X. F. Liang, Y. Zhang, X. Liang, Y. P. Zhu, J. Qin, Y. Gao, B. Peng, N. X. Sun, and L. Bi, Phys. Rev. B **96**, 224403 (2017).

[16] C. Dubs, O. Surzhenko, R. Thomas, J. Osten, T. Schneider, K. Lenz, J. Grenzer, R. Hübner, and E. Wendler, Phys. Rev. Mater. **4**, 024416 (2020).

[17] J. Mendil, M. Trassin, Q. Bu, J. Schaab, M. Baumgartner, C. Murer, P. T. Dao, J. Vijayakumar, D. Bracher, C. Bouillet *et al.*, Phys. Rev. Mater. **3**, 034403 (2019).

[18] A. K. Zvezdin and V. A. Kotov, *Modern Magnetooptics and Magnetooptical Materials* (Taylor & Francis Group, MIlton Park, UK, 1997).

[19] L. Nádvorník, M. Borchert, L. Brandt, R. Schlitz, K. A. de Mare, K. Výborný, I. Mertig, G. Jakob, M. Kläui, S. T. B. Goennenwein, M. Wolf, G. Woltersdorf, and T. Kampfrath, Phys. Rev. X **11**, 021030 (2021).

[20] L. Q. Shen, L. F. Zhou, J. Y. Shi, M. Tang, Z. Zheng, D. Wu, S. M. Zhou, L. Y. Chen, and H. B. Zhao, Phys. Rev. B **97**, 224430 (2018).

[21] M. Montazeri, P. Upadhyaya, M. C. Onbasli, G. Yu, K. L. Wong, M. Lang, Y. Fan, X. Li, P. Khalili Amiri, R. N. Schwartz *et al.*, Nat. Commun. **6**, 8958 (2015).

[22] V. Saidl, P. Němec, P. Wadley, V. Hills, R. P. Campion, V. Novák, K. W. Edmonds, F. Maccherozzi, S. S. Dhesi, B. L. Gallagher *et al.*, Nat. Photonics **11**, 91 (2017).

[23] N. Tesařová, P. Němec, E. Rozkotová, J. Šubrt, H. Reichlová, D. Butkovičová, F. Trojánek, P. Malý, V. Novák, and T. Jungwirth, Appl. Phys. Lett. **100**, 102403 (2012).

[24] J. H. Liang, X. Xiao, J. X. Li, B. C. Zhu, J. Zhu, H. Bao, L. Zhou, and Y. Z. Wu, Opt. Express **23**, 11357 (2015).

[25] G. Chen, J. Zhu, J. Li, F. Z. Liu, and Y. Z. Wua, Appl. Phys. Lett. **98**, 132505 (2011).

[26] W. N. Cao, J. Li, G. Chen, J. Zhu, C. R. Hu, and Y. Z. Wua, Appl. Phys. Lett. **98**, 262506 (2011).

[27] J. Hamrle, S. Blomeier, O. Gaier, B. Hillebrands, H. Schneider, G. Jakob, K. Postava, and C. Felser, J. Phys. D: Appl. Phys. **40**, 1563 (2007).

[28] A. V. Kimel, G. V. Astakhov, A. Kirilyuk, G. M. Schott, G. Karczewski, W. Ossau, G. Schmidt, L. W. Molenkamp, and Th. Rasing, Phys. Rev. Lett. **94**, 227203 (2005).

[29] H. C. Zhao, H. Xia, S. Hu, Y. Y. Lv, Z. R. Zhao, J. He, E. Liang, G. Ni, L. Y. Chen, X. P. Qiu, S. M. Zhou, and H. B. Zhao, Nat. Commun. **12**, 5266 (2021).

[30] P. Němec, V. Novák, N. Tesařová, E. Rozkotová, H. Reichlová, D. Butkovičová, F. Trojánek, K. Olejník, P. Malý, R. P. Campion *et al.*, Nat. Commun. **4**, 1422 (2013).

[31] P. Němec, E. Rozkotová, N. Tesařová, F. Trojánek, E. De Ranieri, K. Olejník, J. Zemen, V. Novák, M. Cukr, P. Malý, and T. Jungwirth, Nat. Phys. **8**, 411 (2012).

[32] N. Tesařová, P. Němec, E. Rozkotová, J. Zemen, T. Janda, D. Butkovičová, F. Trojánek, K. Olejník, V. Novák, P. Malý, and T. Jungwirth, Nat. Photonics **7**, 492 (2013).

[33] T. Hioki, Y. Hashimoto, T. H. Johansen, and E. Saitoh, Phys. Rev. Appl. **11**, 061007(R) (2019).

[34] J. Dillon, J. P. Remeika, and C. R. Staton, J. Appl. Phys. **41**, 4613 (1970).

[35] F. Lucari, E. Terrenzio, and G. Tomassetti, J. Appl. Phys. **52**, 2301 (1981).
[36] F. D'Orazio, F. Lucari, E. Terrenzio, and G. Tomassetti, J. Magn. Magn. Mater. **54**, 1389 (1986).
[37] A. Akbar, M. W. Khalid, and M. S. Anwar, Opt. Express **25**, 30550 (2018).
[38] M. B. Jungfleisch, A. V. Chumak, A. Kehlberger, V. Lauer, D. H. Kim, M. C. Onbasli, C. A. Ross, M. Kläui, and B. Hillebrands, Phys. Rev. B **91**, 134407 (2015).
[39] Z. Frukacz and D. A. Pawlak, *Encyclopedia of Materials: Science and Technology* (Elsevier Ltd., Amsterdam, 2001).
[40] See Supplemental Material at http://link.aps.org/supplemental/10.1103/PhysRevB.106.104434 for details on sample characterization, calculation of the magnetic anisotropy of the YIG film [41], and magneto-optical response of the multilayer [42].
[41] J. F. Dillion, Phys. Rev. **105**, 759 (1957).
[42] F. J. Kahn, P. S. Pershan, and J. P. Remeika, Phys. Rev. **186**, 891 (1969).
[43] P. Hansen, P. Röschmann, and W. Tolksdorf, J. Appl. Phys. **45**, 2728 (1974).
[44] N. Tesařová, J. Šubrt, P. Malý, P. Němec, C. T. Ellis, A. Mukherjee, and J. Cerne, Rev. Sci. Instrum. **83**, 123108 (2012).
[45] S. Lee, S. Grudichak, J. Sklenar, C. C. Tsai, M. Jang, Q. Yang, H. Zhang, and J. B. Ketterson, J. Appl. Phys. **120**, 033905 (2016).
[46] D. D. Stancil and A. Prabhakar, *Spin Waves—Theory and Applications* (Springer, New York, 2009).
[47] Š. Višňovský, *Optics in Magnetic Multilayers and Nanostructures* (CRC Press, Boca Raton, FL, 2006), Chap. 3.
[48] Š. Višňovský, Czech. J. Phys. B **36**, 1424 (1986).
[49] H. S. Wemple, S. L. Blank, J. A. Seman, and W. A. Biolsi, Phys. Rev. B **9**, 2134 (1974).
[50] N. Beaulieu, N. Kervarec, N. Thiery, O. Klein, V. Naletov, H. Hurdequint, G. de Loubens, J. Ben Youssef, and N. Vukadinovic, IEEE Magn. Lett. **9**, 3706005 (2018).
[51] R. Vidyasagar, O. Alves Santos, J. Holanda, R. O. Cunha, F. L. A. Machado, P. R. T. Ribeiro, A. R. Rodrigues, J. B. S. Mendes, A. Azevedo, and S. M. Rezende, Appl. Phys. Lett. **109**, 122402 (2016).
[52] E. Oh, D. U. Bartholomew, A. K. Ramdas, J. K. Furdyna, and U. Debska, Phys. Rev. B **44**, 10551 (1991).
[53] W.-K. Li and G.-Y. Guo, Phys. Rev. B **103**, 014439 (2021).
[54] V. N. Kats, S. G. Nefedov, L. A. Shelukhin, P. A. Usachev, D. V. Averyanov, I. A. Karateev, O. E. Parfenov, A. N. Taldenkov, A. M. Tokmachev, V. G. Storchak, and V. V. Pavlov., Appl. Mater. Today **19**, 100640 (2020).
[55] E. Lišková Jakubisová, S. Višňovský, H. Chang, and M. Wu, Appl. Phys. Lett. **108**, 082403 (2016).